Deep learning based identification of solvents from post-desiccation patterns

J. I. Morán-Cortés* and F. Pacheco-Vázquez

Instituto de Física, Benemérita Universidad Autónoma de Puebla,
Apartado Postal J-48, Puebla 72570, Mexico,
**e-mail: jmoran@ifuap.buap.mx; fpacheco@ifuap.buap.mx*

Received 8 January 2026; accepted 29 May 2026

We introduce an optimized Deep learning protocol for fracture pattern classification to identify the solvent involved in the desiccation cracking process of starch-liquid slurries, even after its complete evaporation. For this purpose, image analysis techniques were used to characterize patterns obtained from drying suspensions using single solvents (water, ethanol, acetone) and two-component solvents (water-ethanol mixtures at different concentrations). Frequency histograms were generated based on nine morphological features, taking into account their size, shape, geometry and orientational ordering. Subsequently, we used these histograms as input data in different artificial neural network variants to determine which set of features leads to the highest accuracy in solvent identification. An average accuracy of up to $96(\pm1)\%$ was achieved in the classification when all solvents were considered in the analysis. The highest accuracy was obtained with sets that include the crack area, $A_{\mathrm{cr}N}$, a feature barely considered in the literature. We found that $A_{\mathrm{cr}N}$ can be related to the cohesive energy associated with hydrogen bond interactions. Taking this into account, we estimated some physicochemical properties of two-component solvents (specifically, the Hansen and Kamlet-Taft parameters) based solely on the features of patterns obtained from the individual components, achieving an error within 15% compared to the values determined from the literature. The proposed protocol could help to encode some implicit parameters and the optimal combination of features for pattern recognition in other fields of science and engineering.

Keywords: Solvent identification; pattern recognition protocol; cracking process; desiccation; neural networks; deep learning.

DOI: https://doi.org/10.31349/RevMexFis.72.061701

1. Introduction

In different scientific fields, neural networks stand out for their effectiveness and efficiency in automatically classifying patterns based on their morphological features [1-10]. Ponomarev *et al*. [4,5] used an automatic classification method of immunofluorescent images for autoimmune disease diagnostics based on the number, size, shape, and localization of individual cells in medical tests, achieving an average accuracy of $84(\pm6)\%$ and showing performance comparable to that of the texture-based method [6]. Umer *et al*. [7] proposed a person identification system based on multiscale morphology to extract structural and textural features from human iris images, with average accuracy of $99(\pm1)\%$. Wang et al. [8] developed a model for material property classification based on X-ray and neutron diffraction patterns of crystal structures, reaching accuracies of $66(\pm14)\%$ for the perovskite family ABO_3. Fan *et al*. [9] propose a model for classifying multi-defect wafer map patterns by combining a densities clustering method with geometric features, including form factor (area/perimeter) and eccentricity, obtaining average accuracy of up to 94%, whereas more recently, Choi and Suh [10] achieved over 98% accuracy for the same purpose with a model focused on the active contour. Although neural networks with statistical approaches are feasible tools for pattern recognition, a correct selection of parameters is essential to avoid overfitting and increase the accuracy and efficiency of the method.

Desiccation patterns are probably the most common examples of how nature spontaneously generates configurations through complex processes that occur over multiple time and length scales. For example, at microscopic scale, slow evaporation of gold nanoparticle suspensions results in microwire patterns induced by drying liquid bridges [11]. Evaporation of blood droplets produces dendritic patterns with radial fissures in the periphery related to a high concentration of lipids [12]. On a much larger scale, drying processes in basins and lakes generate polygonal salt patterns [13], while the shrinkage of frozen ground (permafrost) creates ice-filled crevices and soil [14]. Furthermore, these polygonal patterns are not limited to Earth alone, but are also found on the surface of Mars [14-19] and the Moon [17]. Such patterns exhibit great morphological diversity due to the influence of multiple factors during their formation; however, they can be effectively analyzed and classified using image analysis and Deep learning techniques (for example, to predict the number of cracks in the soil based on the initial moisture content, layer thickness, and sample size [20]), provided that adequate selection of parameters is made.

Thin layers of colloidal suspensions have been extensively used at laboratory scale to explore desiccation processes. On the one hand, it has been shown that the morphology of the resulting cracking patterns depends significantly on the thickness h of the layer. Theoretically, thin films crack upon reaching a critical stress, which relaxes over a distance proportional to h [21], while the crack spacing L follows a power scaling with exponent $n = 2/3$ [17,22], in reasonable agreement with experiments ($n = 0.65 \pm 0.01$ for silica particles [23,24], $n = 0.71 \pm 0.01$ for cornstarch and $n = 0.53 \pm 0.02$ with clay [17]), for which the character-

istic lengths $L_1 = \sqrt{A_c/N_c}$ and $L_2 = A_c/L_T$ have been proposed, where A_c is the size of the container, N_c the number of cells, and L_T the total length of the cracks. In addition, the average displacement of the pattern vertices increases linearly with h during repeated wetting and drying cycles [21]. Likewise, the characteristic area A of the patterns is directly proportional to $h^{4/3}$ when using cornstarch with water, as well as calcium carbonate $(CaCO_3)$ with different solvents such as water, isopropanol and silicone oil [16,17]. On the other hand, Choudhury *et al.* [25] studied the desiccation cracking process in bentonite-chloride salt slurries. Bentonite can exhibit strong swelling and dispersion due to water absorption, but the presence of dissolved salts affects shrinkage properties, surface tension and internal stress distribution by altering the ionic concentration, osmotic effects, and physicochemical properties. All these results evidence the influence of solute/solvent interactions on the morphological features of fracture patterns.

In order to classify fracture patterns, frequency histograms are a useful tool to represent their morphological distribution. A variety of parameters exists to characterize the geometry and topology of these patterns based on radial density profile [12], average areas [16,26-29], lengths [17,19,23,24,27,30], number of neighbors [19,29,31], fractal dimension [32,33] and lacunarity [33], to name a few, but only some studies include a large dataset of measurements. However, histograms based on the normalized isoperimetric ratio, defined as $\lambda = 4\pi A/P^2$, where A is the area and P is the perimeter of the patterns, have been proposed by Roy *et al.* [29] as the most efficient parameter to distinguish between fracture patterns, which they qualitatively evidenced in cracked materials of natural mud, clays (such as laponite and bentonite), corn and potato starch extracts, polymers (such as PDMS), among others. From a statistical point of view, this should hold true even if the successive cleavage of the fracture patterns does not follow a regular or uniform process [31]. For this reason, histograms of the area−perimeter set and other morphological features may contribute to the automated identification of such patterns, but the effectiveness and efficiency of these features for classification is still unknown.

In this work, we propose an optimized Deep learning protocol that uses neural networks to recognize and classify fracture patterns produced during the desiccation of cornstarch-liquid slurries involving different solvents. For this purpose, an experimental array (described in Sec. 2) was used to follow the evaporation process of thin layers of the slurries until the fracture patterns appear. The experimental results are discussed in Sec. 3. The methodology used for the morphological analysis is described in Sec. 4, where the set of features are represented in frequency histograms to characterize fracture patterns from their size, shape, geometry and orientational ordering. On the one hand, the size is characterized using the area and perimeter of the cells and the area of the cracks, all normalized by characteristic values, while shape is described by the eccentricity. On the other hand, the geometry is determined by the number of neighbors, obtained from Voronoi diagrams; while ordering is determined by an order parameter, defined as a function of these neighbors and the centroids of the cells. In Sec. 5, we outline the framework of the proposed protocol, emphasizing the construction, training, and accuracy calculation of an Artificial Neural Network (ANN) to classify experimental sample classes. Subsequently, in Sec. 6, the accuracy of the classification was evaluated considering each individual feature as well as combinations of different sets of features, identifying those sets that lead to the highest accuracies. We also discuss why the feature A_{cr} becomes relevant for the classification based on its correlation with hydrogen bonding solute-solvent interactions. In Sec. 7, a possible application of the protocol focused on the estimation of physicochemical properties is presented. The conclusions are finally summarized in Sec. 8. Additionally, an Appendix section is provided to explain why the accuracy of the model can be compromised in the analysis.

2. Experimental setup

The experimental design is sketched in Fig. 1a), and it is similar to previous systems used in the literature [26,27]. A given mass of cornstarch-liquid slurry is deposited in a cylindrical aluminium container of diameter $D_c = 100$ mm, and the container is placed on an analytical balance (OHAUS PX423). The system allows for recording the mass of the slurry during the desiccation process every minute, and a digital thermometer-hygrometer placed inside the balance chamber was used to register the temperature $T\,(^\circ\mathrm{C})$ and the relative ambient humidity RH $(\%)$ every five minutes. A digital camera (NIKON D3200) is positioned to record images from a top view of the container and to capture the final morphology of the fracture patterns.

The mixtures were prepared with an initial concentration $\phi_0 = 1/2$, defined as $\phi_0 = m_{liq}/\,(m_{liq} + m_{cs})$ [34], where m_{liq} is the mass of the liquid (solvent) and m_{cs} corresponds to dry cornstarch (solute), obtained from a commercial brand (Maizena). A mass $m_0 = 40.0\,(\pm 0.1)$g of the homogeneous mixture was prepared for each experiment using equal masses of liquid (20.0g) and cornstarch (20.0g), obtaining average densities $\rho = 1.20(\pm 0.01)\,\mathrm{g/cm^3}$ for cornstarch-

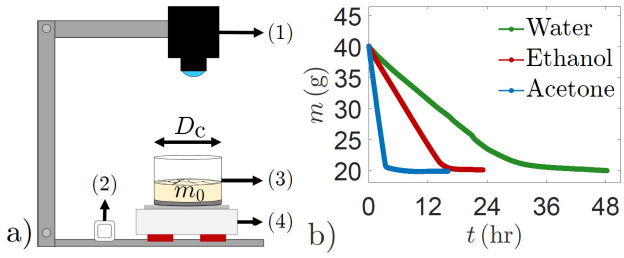


FIGURE 1. a) Experimental setup components: (1) digital camera, (2) digital thermometer-hygrometer (3) aluminum container with initial mass m_0 of a specific mixture, and (4) analytical balance. b) Remanent mass m of the mixtures as a function of time t during the drying process, for three different solvents.

water slurry and $\rho = 1.03(\pm 0.01)\,\mathrm{g/cm^3}$ for both cornstarch-ethanol and cornstarch-acetone slurries. The mixture is deposited in the center of the container, and it extends radially, forming a thin horizontal liquid layer of thickness $h_0 \sim 4-5\,\mathrm{mm} \ll \mathrm{D_c}$. Once the solvent evaporation is completed, the layer thickness (and therefore, the volume of the layer) is reduced by $16(\pm 1)\%$, and the patterns are recorded for subsequent analysis.

Following the procedure described above, 75 liquid layers were prepared using single solvents, distributed in 25 samples for each solvent: deionized water, ethanol (CTR Scientific) and acetone (CTR Scientific). The samples were left to evaporate naturally for 48, 24, and 12 hours for the water, ethanol, and acetone mixtures, respectively. The latter substances are more volatile and require less time for total evaporation, which is considered to occur when $m \approx 20$ g, *i.e.* when all the liquid has been evaporated and only the solute remains in the container. Environmental conditions remained nearly constant throughout the experiments, with an average relative humidity of $\mathrm{RH_{env}} = 39(\pm 6)\%$ and an average room temperature of $T_{\mathrm{env}} = 28(\pm 1)^{\circ}\mathrm{C}$.

3. Experimental results

3.1. Evaporation process

Figure 1b) shows how the mass of the mixture m decreases with time t for the three samples of water, ethanol and acetone. From the moment of deposition, evaporation proceeds in two stages [26,35,36]. First, the mass decreases linearly with time (constant evaporation rate) until a wet cornstarch layer seems to settle at the bottom of the container, which is characterized by the notorious change of curvature in the plots. At this moment, the layer adheres to the substrate and begins to contract until it detaches from the container walls. This process is consistent for different solutes in water, such as cornstarch [16,30], granular polymers [37], Romainville clay [27], hard and soft nanolatex spheres [26,31], Sisal fiber and soil [38], sand and kaolinite clay [32], among others. Subsequently, two types of cracks appear that divide the layer into primary and secondary patterns according to their order of appearance [16,30]. Primary patterns arise from a critical h_c layer thickness and they are formed in the first evaporation stage due to capillary contraction of the material [16]. During the second evaporation stage for the case of cornstarch in water, secondary patterns emerge in large amounts and simultaneously within the primary patterns due to dehydration of the hygroscopic cornstarch particles [16,31], even when the layer thickness is $h < h_c$. For the case of ethanol and acetone, only one kind of cracks appear during the evaporation process and the resulting patterns are more homogeneous, as we discuss in the following section.

3.2. Fracture patterns produced by different solvents

Figure 2 shows that the final fracture patterns depend on the solvent used. For the case of water, primary thicker fractures are clearly observed (secant lines crossing almost the whole layer), which are not observed with ethanol or acetone. There are also numerous small secondary thinner fractures associated with columnar joints in water [21,35,36], while the number of cells decreases significantly in ethanol and acetone, causing an increase in their size, as shown in Fig. 2a). Furthermore, the secondary cells are larger in acetone than in ethanol, whereas in water they are noticeably smaller and more irregular. Consequently, the samples in Fig. 2a) can in principle be easily distinguished from one another.

The change in pattern features can be associated to changes of the physicochemical properties of the solvent. To explore this aspect, we considered 50 additional liquid layers with binary solvents consisting of mixtures of water and

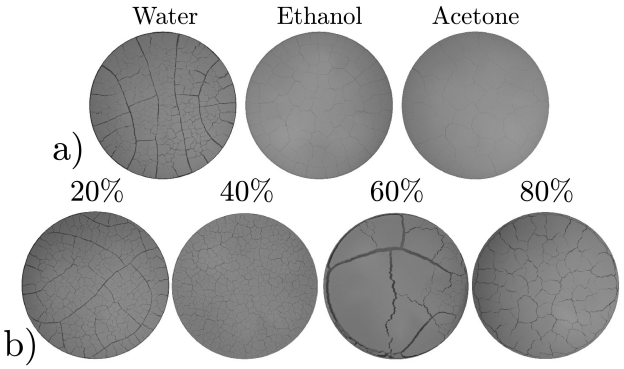


FIGURE 2. Fracture patterns observed in experimental samples of mixtures using solvents of a) pure liquids and b) water-ethanol mixtures with the indicated percentages of ethanol.

TABLE I. Some properties of pure solvents and ethanol-water binary solvents used in this study, including: the surface tension σ, density ρ and viscosity η at $25^{\circ}\mathrm{C}$ [39-43]. Volume fraction v and mole fraction X of ethanol ($M = 46.07$) in water ($M = 18.02$), depending on the indicated percentage of ethanol mass in the mixture, where M denotes the molar mass.

Property	Water	20%	40%	60%	80%	Ethanol	Acetone
σ (mN/m)	72.01	37.97	30.16	26.23	23.82	21.82	23.02
ρ (g/cm^3)	0.9971	0.9663	0.9316	0.8882	0.8398	0.7856	0.7843
η (mPa·s)	0.8907	1.7803	2.3586	2.2411	1.7302	1.0907	0.3050
v	0	0.241	0.458	0.656	0.835	1	-
X	0	0.089	0.207	0.370	0.610	1	-

ethanol at different concentrations (see Table I). The characteristic patterns of the transition from pure water to pure ethanol are shown in Fig. 2b) using water-ethanol mixtures at 20, 40, 60 and 80 % of ethanol content. On the one hand, for concentrations close to pure liquids, the number of patterns and the size of the cracks appear similar to those of the dominant liquid, although contrasting morphological features arise due to the recessive liquid. On the other hand, mixtures with comparable proportions of water and ethanol can be clearly distinguished from the other samples. For instance, at 40% ethanol, primary cracks disappear with respect to 20%, but the number of secondary cells looks similar. A particular pattern appears at 60% ethanol, in which case the pattern size and width of the cracks seem considerably larger. However, in the mixture of 80% ethanol, a clear competition arises between the morphological features obtained with pure liquids; the presence of water produces thicker fractures, but with an ordering and geometry of cells similar to those observed in pure ethanol. Therefore, the number of patterns, the spatial distribution, their average area and perimeter, and the thickness of the cracks are morphological features of the patterns determined by the solvent, which have to be considered in the classification and identification protocol.

4. Morphological analysis

Figure 3 illustrates the methodology used for the morphological analysis of fracture patterns. Images of all experimental samples are first captured, as illustrated in Fig. 3a). Then, using the software FIJI ImageJ®, each image is binarized to show exclusively the cracks that outline the boundaries of the patterns as depicted by the red borders in Fig. 3b). By performing this image analysis iteratively for each of the experimental samples, five main features can be estimated: the number $N_{\rm c}$ of patterns in each experimental sample, the area A, perimeter P, centroid $C\,(x,y)$, and eccentricity ε of the patterns. After applying Voronoi tesselation, the total length $L_{\rm T}$ was obtained. Furthermore, each image was divided in $n = 64$ circular sectors to account for variations in the crack distribution, and the number of pixels conforming the cracks in each sector was estimated, which allows to obtain the area $A_{\rm cr}$ of the cracks. These morphological features characterize the size (area−perimeter) and shape (eccentricity) of the fracture patterns.

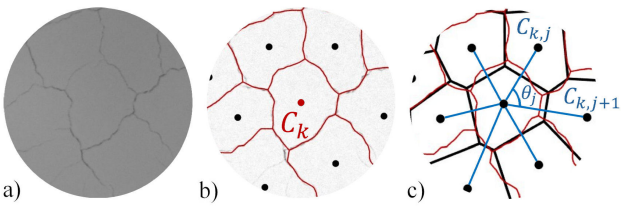


FIGURE 3. Image processing. a) Picture of a fracture pattern. b) Corresponding centroids (black dots) and c) Voronoi diagram (black edges) from the real fracture pattern (red edges) after image processing.

On the other hand, centroids [Fig. 3b)] allow to infer geometrical and ordering features of the patterns, which show a high correspondence with the Voronoi diagrams [black edges in Fig. 3c)] [29]. Using MATLAB®, if we focus on the Voronoi diagram of the centroid C_k of some pattern [see Fig. 3b)], we can compute its number of neighbors $N_{{\rm B},k}$ with the associated Voronoi diagram to know its geometry. In addition, such centroid can be linked to two adjacent and consecutive centroids $C_{k,j}$ and $C_{k,j+1}$ by straight lines [blue lines in Fig. 3c)] to calculate the angle θ_j between them. Therefore, the associated bound orientational parameter (BOP) $\psi_{k,n}$ of each $k-$th pattern [44], defined as a function of the number $N_{{\rm B},k}$ and the angles θ_j for each $j = 1, \ldots, N_{{\rm B},k}$, can be computed by:

$$\psi_{k,n} = \frac{1}{N_{{\rm B},k}} \left| \sum_{j=1}^{N_{{\rm B},k}} \exp\left(in\theta_j\right) \right|, \quad 0 \leq \theta_j < 2\pi, \tag{1a}$$

with

$$\theta_j = \arccos\left[\frac{(C_{k,j+1} - C_k)\cdot(C_{k,j} - C_k)}{|C_{k,j+1} - C_k|\cdot|C_{k,j} - C_k|} \right]. \tag{1b}$$

By applying the morphological analysis to all fracture patterns, we initially estimate the average values of such morphological features. On the one hand, since the area of the container $A_{\rm c} = 7854$ mm^2 is constant, then the average area $\overline{A}$ of the patterns is inversely proportional to $\overline{N}_{\rm c}$, such that: $\overline{A} \approx A_{\rm c}/\overline{N}_{\rm c} = L_1^2$. On the other hand, the measurements obtained from the image analysis also reveal that $\overline{P} \approx 8A_{\rm c}/\overline{L}_T = 8L_2$. Additionally, the patterns exhibit similar characteristics; they follow the normalized isoperimetric ratio with an average value of $\lambda = 0.70 \pm 0.03$, and they show comparable average values of eccentricity ($\varepsilon = 0.67 \pm 0.07$) and order parameter ($\psi = 0.47 \pm 0.17$). Therefore, normalized quantities for the sizes of the patterns and cracks can be defined relative to these characteristic lengths, *i.e.*, $A_{\rm N} = A/L_1^2$, $P_{\rm N} = P/\left(8L_2\right)$, and $A_{{\rm cr}N} = A_{\rm cr}/L_3^2$, respectively, where $L_3 \equiv L_1^2/L_2 = L_T/N_{\rm c}$. Then, a set of normalized features can be used for the morphological characterization of the fracture patterns.

Figure 4 displays the size and shape measurements in the form of frequency histograms of normalized features, which help to identify those parameters that can be useful to classify the experimental samples. To obtain the histograms, the methodology described above was iteratively applied to the samples [see Figs. 4A)-4B)], with the goal of extracting and characterizing nearly $24,000$ individual cells. In the histograms, one can notice that the measurements for ethanol are more homogeneous than for the case of water (which shows a wider distribution). For the mixture of 20% water and 80% ethanol, two maxima appear in the distributions of $A_{\rm N}$ and $P_{\rm N}$ indicating a superposition of the effects of both solvents. There is also a noticeable shift to the left in the maximum of the $A_{{\rm cr}N}$ distribution for more volatile liquids. This indicates thinner cracks for acetone and ethanol compared to water.

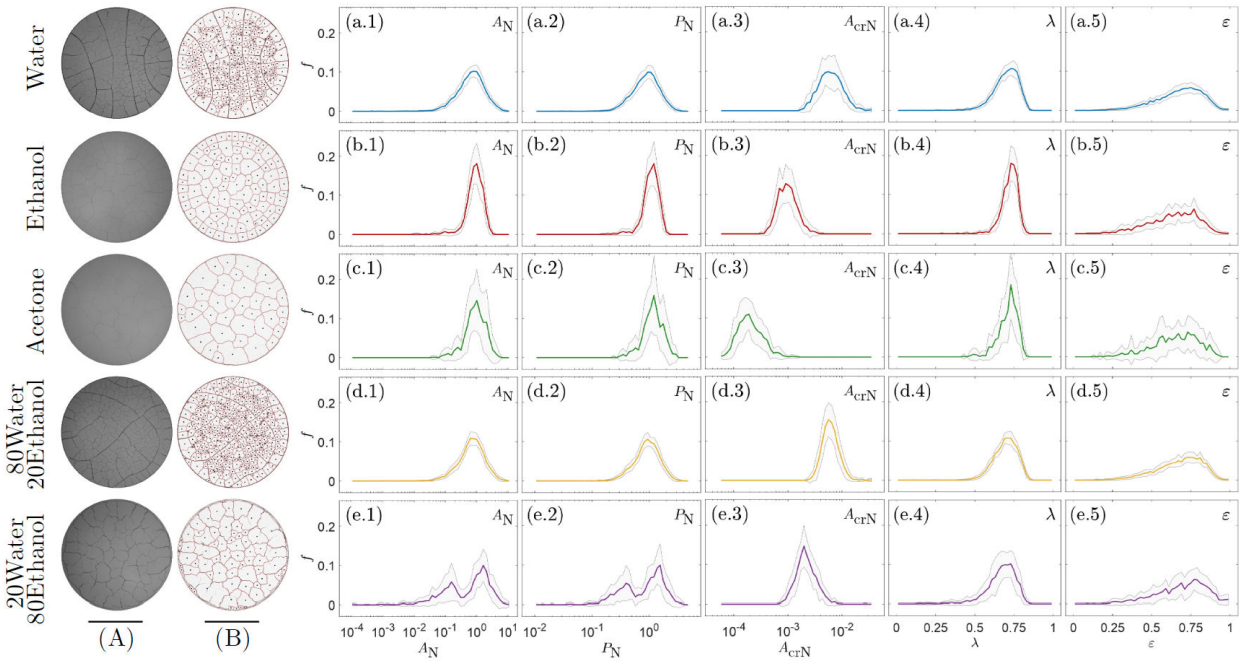


FIGURE 4. Size-shape analysis. (A) Final patterns observed after the desiccation process of layers of cornstarch and the indicated solvent. (B) Corresponding processed images used to identify the cracks (red edges) and their centroids (black dots). In A and B the scale bar is 50 mm. (a-e) Histogram distribution of (1) pattern area A_N, (2) perimeter P_N, (3) crack area A_{crN}, (4) isoperimetric ratio λ, and (5) eccentricity ε, obtained using as solvent: (a) water, (b) ethanol, (c) acetone, and (d) $80/20\%$ and (e) $20/80\%$ water/ethanol. Colored lines represent the average value and the gray shaded area represents the standard deviation.

For the binary mixtures, the maximum is between the values corresponding to the pure solvents, and the shift depends on the ethanol concentration, suggesting that A_{crN} could be one of the most relevant parameters for the classification and identification of the solvents.

Figure 5 shows histograms corresponding to ordering parameters (ψ_4, ψ_5, ψ_6) and number of neighbors N_B, where it is more difficult to distinguish by eye the differences between the distributions. The histograms show that the patterns have between 4 and 7 neighbors, while on average they tend toward hexagonal geometries $(N_B = 6 \pm 1)$ in samples with pure water and, 80% water and 20% ethanol mixture, but they tend toward pentagonal geometries $(N_B = 5 \pm 1)$ in those with pure ethanol, pure acetone and, 20% water and 80% ethanol mixture [see Fig. 5A)]. On the other hand, the order parameter is used to analyze whether the centroids of the patterns are organized in an ordered $(\text{BOP} \to 1)$ or disordered $(\text{BOP} \to 0)$, but from Figs. 5A)-5D) one finds that the $47\,(\pm 2)\,\%$ of the patterns present values of BOP between 0.35 and 0.65 [see Fig. 5B)], which are around their mean value; therefore, it is concluded that the centroids do not manifest a predominant symmetry associated with square, pentagonal or hexagonal structures.

5. Deep learning implementation

Let us now describe the Deep learning approach used to identify the solvent involved in the desiccation process (see framework in Fig. 6). First, we apply the fracture pattern analysis described in the previous section to obtain the frequency histograms [Fig. 6a)]. Then, the Artificial Neural Networks (ANNs) is trained in MATLAB® using a 5-fold cross-validation [Fig. 6b)], where the dataset is divided into five equal parts: four of them (80%) are used as the training set, and the remaining one (20%) as a test set (shown in yellow), and the latter is rotated until all five possible combinations are covered [10,45]. Then, a multilayer perceptron (MLP) neural network with a given number of neurons N is employed, which consists of fully connected layers: an input layer (IL), one or more hidden layers (HL $= 1 - 10$), and an output layer (OL). Here, the frequency histograms are used as input data $(f_1, f_2, \ldots, f_n)$ and the different solvents are defined as output data $(C_1, \ldots, C_5)$. Subsequently, the neural network is trained using the Scaled Conjugate Gradient (SCG) backpropagation algorithm, which iteratively adjusts weights and biases to minimize errors, with three predefined random seeds to ensure the reproducibility. For each hidden layer, the hyperbolic tangent sigmoid function $\tanh(x) = 2/(1 + \exp(-2x)) - 1$ is used as the activation function, while the softmax transfer function $y_i = \exp(x_i)/\left[\sum_{j=1}^{N} \exp(x_j)\right]$ is assigned to the output layer. Using an initial number of neurons N, ranging from 60 to 120 in increments of 2 neurons, 31 neural network variants are evaluated for each individual feature $\{X_1, \ldots, X_9\}$ across ten hidden layers with steps of $p = 6$ neurons. The confusion matrix highlights the correctly classified samples (shown in

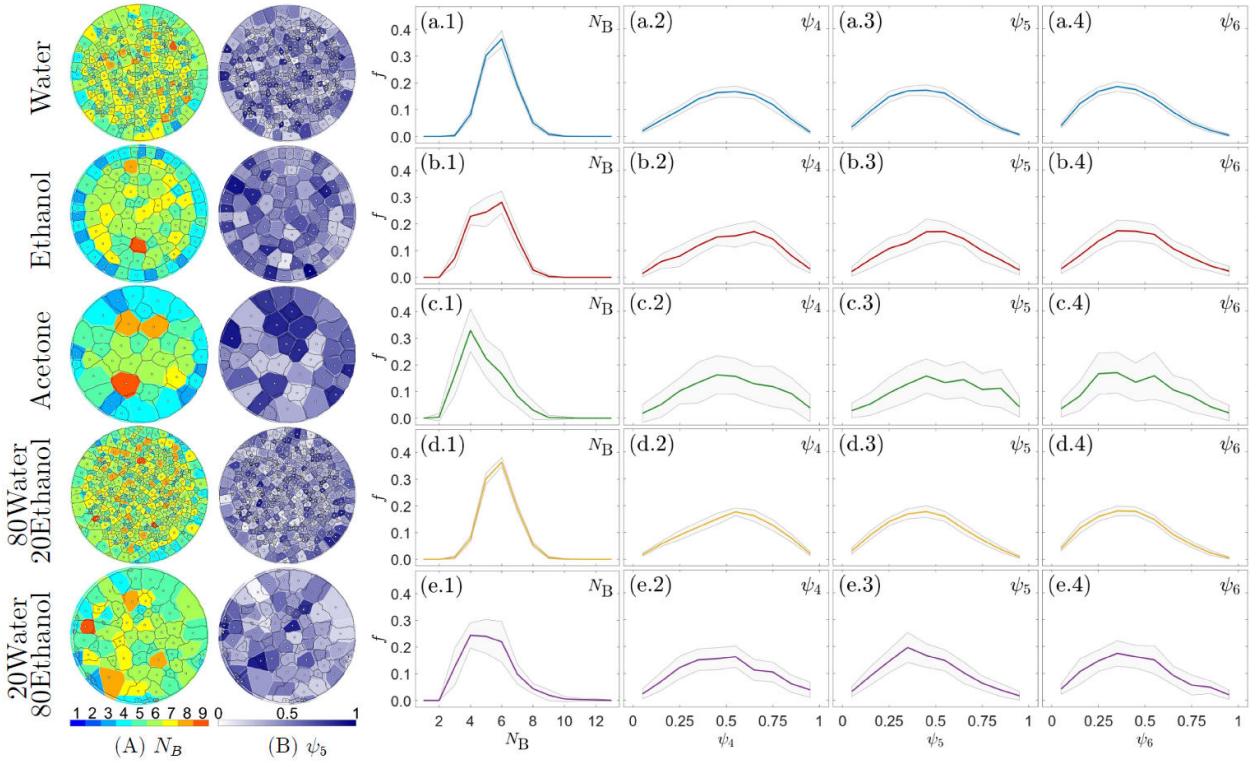


FIGURE 5. Orientational ordering analysis. (A-B) Voronoi diagrams (colored cells) and centroids (white dots) obtained from the actual patterns (black lines) depending on the solvent. Colors are used to indicate A) the number of neighbors N_B and B) the orientational order (here ψ_5 is shown for visualization) according to the color bars. (1-4) Frequency histograms of 1) nearest neighbors, and different order parameters 2) ψ_4, 3) ψ_5 and 4) ψ_6, depending on the solvent indicated in the same row. Colored lines represent the mean values and the gray shaded areas the corresponding standard deviations.

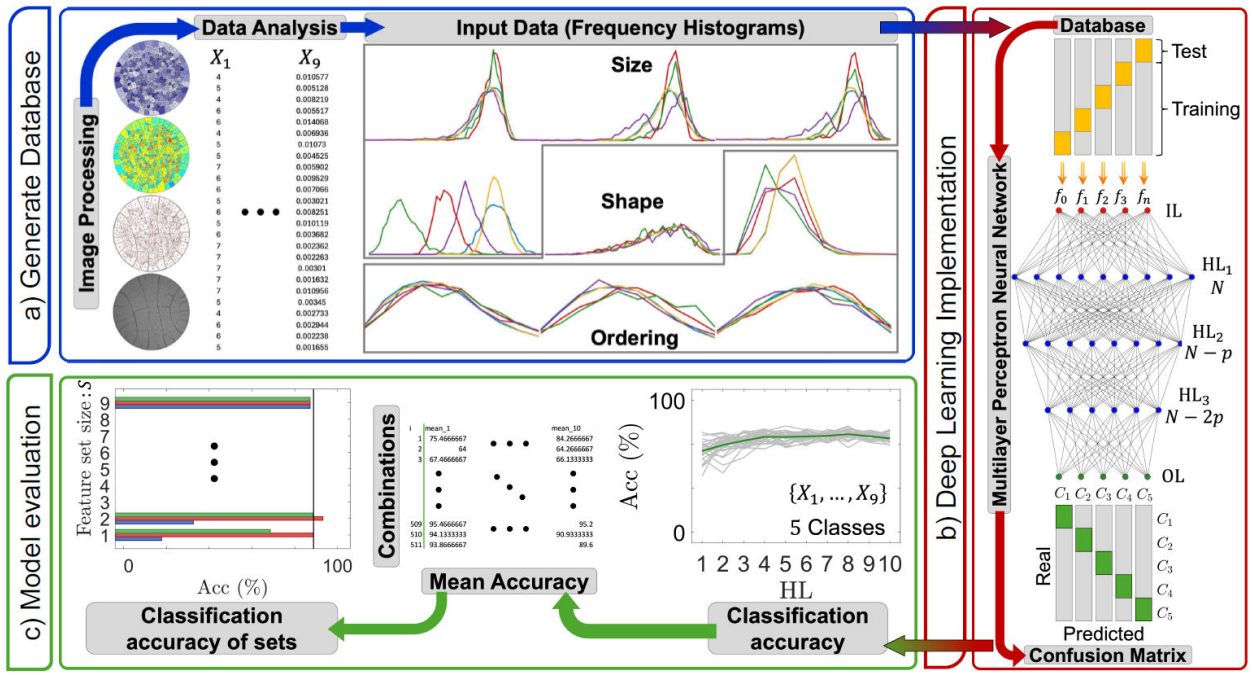


FIGURE 6. Framework of the proposed protocol, including: a) database construction, b) Deep learning implementation, and c) model evaluation.

green), which vary for each neural network variant, and the classification accuracy is calculated as the ratio of the number of correct predictions to the total number of tests. While the mean diagonal of the confusion matrix is used to determine the accuracy, the model confusion is given by the off-diagonal elements. From 465 runs per hidden layer (5 folds $\times$ 3 seeds $\times$ 31 variants), an average accuracy curve is obtained, illustrated by the green curve of the Acc vs HL plot in Fig. 6c). This process is performed with all the size, shape, and ordering features to determine which of them lead to a higher classification accuracy, individually or forming feature sets of different size $(S = 1, \ldots, 9)$.

6. Model evaluation

6.1. Accuracy of individual features

Figure 7 shows the variation in the accuracy of the classification as a function of the number of hidden layers. The upper curves (higher accuracy) in each plot correspond only to

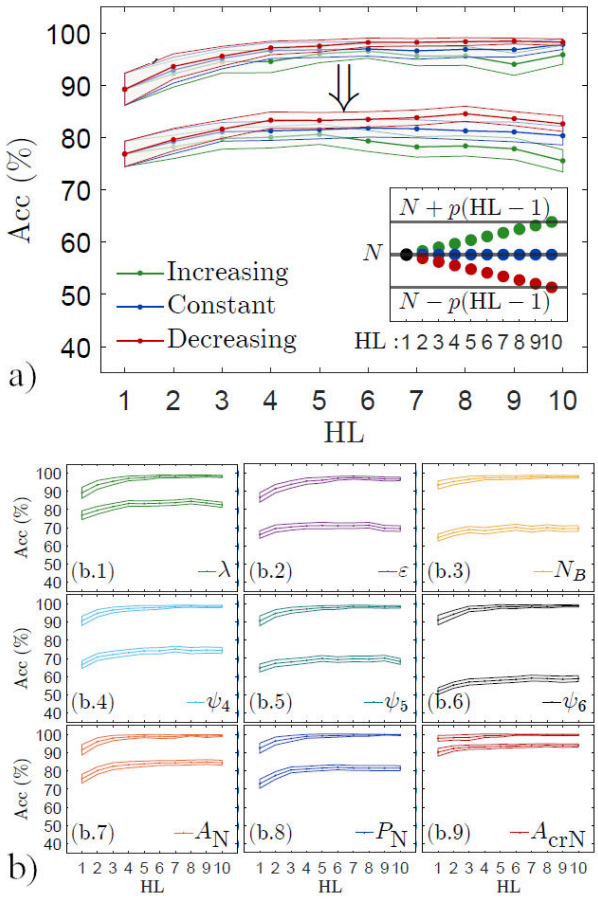


FIGURE 7. Classification accuracy. Performance of a) the normalized isoperimetric ratio λ in three MLP neural network configurations depicted in the inset: increasing, constant, and decreasing architectures as a function of the number of hidden layers (HL). b) Performance of each feature in the decreasing architecture. Solid lines indicate mean values, and shaded areas represent the corresponding standard deviations.

the classification of single solvents (water, ethanol, and acetone), while the bottom curves (lower accuracy) also include binary solvents. In particular, using the isoperimetric ratio, Fig. 7a) exemplifies the accuracy reached for three MLP neural network configurations obtained by decreasing, keeping constant, or increasing the number of neurons in each hidden layer (as shown in the inset). One can notice that the decreasing MLP neural network achieves the highest accuracy [red symbols in Fig. 7a)]. Thus, we can improve the accuracy of the classification by choosing this architecture, which is the one used in the rest of this study. The decrease of accuracy when binary solvents are included is due to an increase on confusion in the analysis generated by the overlapping of the frequency histograms and the similar microscopic physicochemical properties of the solvents (see Appendix section).

Figures 7b) present a comparison of the classification accuracy achieved using nine individual features $(\lambda, \varepsilon, N_{\mathrm{B}}, \psi_4, \psi_5, \psi_6, A_N, P_N, A_{\mathrm{crN}})$ as input to the 31 variants of the decreasing MLP neural network, in order to identify those parameters contributing to higher or lower predictive performance. When all the solvents are included (lower curves), the order parameter ψ_6 yields the lowest performance, with accuracies ranging from $51(\pm2)\%$ to $59(\pm2)\%$; ε,N_{B}, ψ_4 and ψ_5 achieve values from $64(\pm2)\%$ to $75(\pm2)\%$. In comparison, the normalized parameters λ, P_N and A_N reach higher values from $73(\pm3)\%$ to $85(\pm1)\%$. Notably, the normalized crack area A_{crN} yields the highest performance, ranging from $90(\pm2)\%$ to $94(\pm1)\%$; therefore, this is a key parameter to maximize the accuracy of the classification.

6.2. Improving accuracy with set of features

The combination of features can be used to improve even more the classification accuracy, using concatenated histograms as input data of the decreasing MLP neural network. By combining the features, there are $2^9 - 1 = 511$ possible sets with at least one feature. Thus, we calculated the average accuracy of each combination to identify the set of features that maximizes the accuracy, and avoid sets with overfitting that decrease its overall value. Figure 8 presents those sets with the lowest (blue), intermediate (green) and highest (red) average accuracies, depending on the number of parameters conforming the set. For the case of single solvents [Fig. 8a)], the combination of parameters leads to very high accuracies $> 95\%$. Even with a two-feature set $(\psi_4, A_{\mathrm{crN}})$, the highest accuracy is reached (100.0%), but using the full nine-features set results in overfitting, with a slight decrease of accuracy and inconvenient longer processing time. On the other hand, including binary solvents in the analysis [see Fig. 8b)], the classification is certainly less accurate. In this case, the two-feature set (ψ_5, ψ_6) yields the lowest classification performance, with an accuracy of $66.1(\pm2.8)\%$. In contrast, the four-feature set $(\lambda, \psi_4, \psi_5, A_{\mathrm{crN}})$ yields the highest accuracy of $97.0(\pm1.2)\%$, slightly better than the two-feature set $(\psi_4, A_{\mathrm{crN}})$, which accuracy is $96.8(\pm1.4)\%$. The use of all the parameters also results in overfitting in this case, with

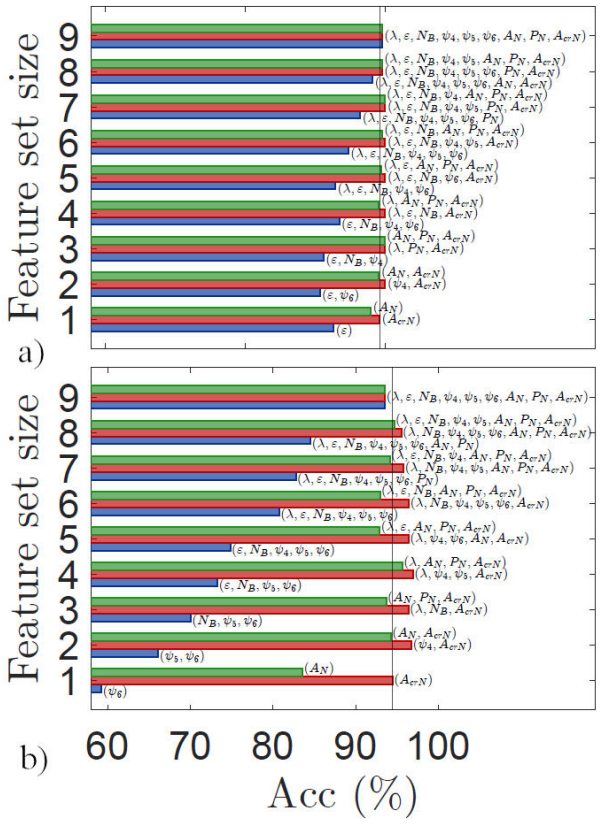


FIGURE 8. Classification accuracy for some sets of features (with $N = 60$ neurons), comparing a) three classes corresponding to single solvents (water, ethanol, and acetone) and b) five classes including the single solvents and binary solvents (20% and 80% ethanol content in water). For sets with the same number of elements, the worst, intermediate and best accuracies are indicated by blue, green and red bars, respectively. For comparison, green bars correspond to the same sets in both cases a) and b). The vertical black line corresponds to the accuracy using only $A_{\mathrm{cr}N}$, which leads to the highest value obtained with an individual feature.

an accuracy of $93.6(\pm 1.6)\%$. Therefore, the most suitable set of features for the classification in both groups of solvents is $(\psi_4, A_{\mathrm{crN}})$, associated with the orientational ordering and the area of the cracks. It is important to remark that the measurement and subsequent analysis of data is simpler for those features that can be easier to determine. For instance, an adequate feature set to analyze unknown samples of fractured dried layers that requires less processing time is the set associated with size $(\lambda, A_N, P_N, A_{\mathrm{cr}N})$ which achieves an average accuracy of $96(\pm 1)\%$, very close to the highest value.

6.3. What makes A_{cr} a powerful feature for pattern classification? Towards a microscopic perspective

In the previous sections, we show that A_{cr} can perform better as a morphological feature for classification than most of features sets, and those sets leading to higher accuracy also include A_{cr}. In order to understand why this parameter plays such a fundamental role in the classification, it is necessary to discuss the origin of crack formation and the role of physicochemical properties involved in the process.

The consolidation of particles during the evaporation of colloidal and granular suspension produces an increase of the tensile stresses due to the competition between the compressive capillary pressure and substrate constraints [46], nucleating cracks to dissipate stored elastic energy. This process is fundamentally governed by the Griffith's criterion [21,47-49]. According to this criterion, primary cracks form in the direction that maximizes the condition: $\mathcal{G} - \mathcal{G}_c \geq 0$, where $\mathcal{G}$ is the strain energy release rate and $\mathcal{G}_c$ denotes the critical energy required to create new fracture surfaces. The critical value $\mathcal{G}_c$ depends on the surface energy per unit area γ_s and the plastic work per unit area γ_p [49].

In our system of cornstarch-water slurries, both primary and secondary cracks are observed. This is in agreement with previous studies [16,28]. Thick primary cracks appear first sequentially, while thinner secondary cracks appear later simultaneously within primary cells. The first ones typically form T-junctions, while the second ones form Y- or V-junctions. According to Refs. [16,28], capillary-induced film shrinkage promotes primary cracks. As the water evaporates, solvent menisci form between individual particles, generating a Laplace pressure that scales as $\Delta P \sim \sigma/R$, where $R \sim 6\ \mu$m is the mean size of cornstarch particles [16,28]. Therefore, the induced capillary stress is ~ 12 kPa. The secondary cracks are generated by the deswelling of the hygroscopic cornstarch particles [16]. In contrast, only one kind of cracks is observed for cornstarch with ethanol or acetone ($\sigma \sim 22$ mN/m), where the induced capillary stress (~ 4 kPa) is not enough to generate large primary cracks. Similar results were found for potato starch in water [28], where primary cracks are suppressed and only secondary cracks are formed, in which case, the reduction in capillary stress comes from the particle size ($R \sim 15\ \mu$m). Since primary cracks disappear using binary solvents between the range of 20-40 % of ethanol in water mixtures ($\sigma \sim 30-38$ mN/m), one can roughly estimate a critical stress of ~ 6 kPa. Additionally, we have to consider that changes in the rheology of the suspension could contribute to generate changes in the observed patterns. It was recently reported that the suspension behavior changes continuously with ethanol concentration from dynamic shear thickening for pure water to low viscosity shear thinning for pure ethanol, passing through a yield-stress-fluid phase for intermediate mixtures, with a maximum solubility (cosolvency effect) at 50-75% concentration [50]. This effect could be associated to the remarkable change in the pattern at 60% concentration in Fig. 2.

The above discussion suggests that changes in desiccation patterns for the cornstarch slurry could be mainly due to surface tension and solubility effects, which are determined by atomic and molecular interactions within the material. At atomic and molecular scales, solute-solvent interactions results in cohesive energy. In cornstarch-liquid slurries, starch (mainly amylose and amylopectin [51,52]) contains hydroxyl groups that form strong hydrogen bonds [53] with solvents

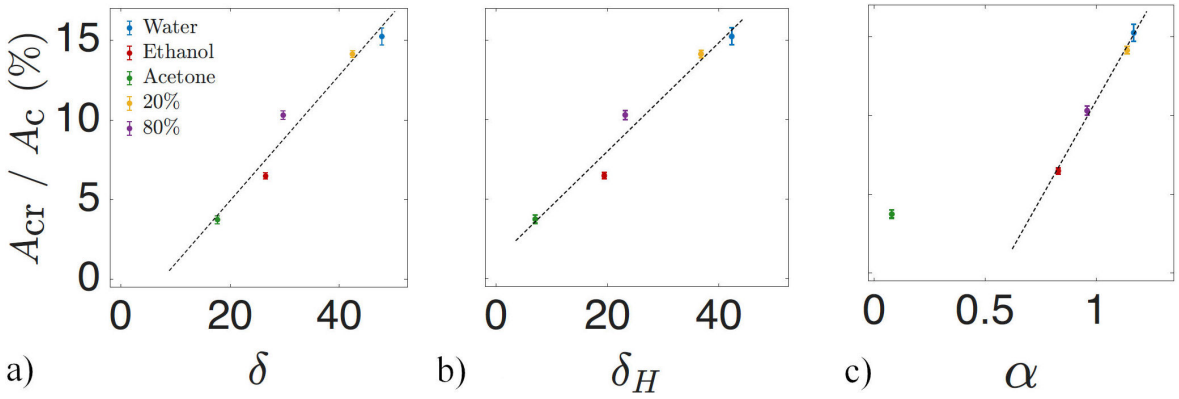


FIGURE 9. Crack area values per solvent. Crack area A_{cr} normalized to container size $A_c = (\pi/4)D_c^2$ with respect to a) Hildebrand parameter δ b) Hydrogen bonding, δ_H (Hansen parameter), and (c) hydrogen-bond donor, α (Kamlet-Taft parameter). Linear fits of experimental data corresponding to a) $(A_{cr}/A_c)\times 100\% = 0.39\,\delta - 2.95$, b) $(A_{cr}/A_c)\times 100\% = 0.34\,\delta_H + 1.19$, and c) $(A_{cr}/A_c)\times 100\% = 24.86\,\alpha - 13.94$.

TABLE II. Hansen parameters δ_D, δ_P and δ_H [54], and Kamlet-Taft parameters α, β and π^* [55,56] of the indicated pure solvents and ethanol-water binary solvents. The corresponding parameters for binary solvents were calculated using the linear approximation: $\delta_{i,\text{mix}} = v\delta_{i,\text{ethanol}} + (1-v)\delta_{i,\text{water}}$ [54] and $\kappa_{\text{mix}} = X\kappa_{\text{ethanol}} + (1-X)\kappa_{\text{water}}$, with $i \in \{D, P, H\}$ and $\kappa \in \{\alpha, \beta, \pi^*\}$ [56], with the values of v and X for ethanol in water provided in Table I.

Property	Water	80/20%	20/80%	Ethanol	Acetone
δ_D (MPa$^{1/2}$)	15.50	15.57	15.75	15.80	12.50
δ_P (MPa$^{1/2}$)	16.00	14.27	9.98	8.80	10.40
δ_H (MPa$^{1/2}$)	42.30	36.78	23.17	19.40	7.00
δ (MPa$^{1/2}$)	47.81	42.42	29.74	26.52	17.70
α	1.17	1.14	0.96	0.83	0.08
β	0.18	0.23	0.54	0.77	0.48
π^*	1.09	1.04	0.75	0.54	0.71

with high hydrogen-bonding parameters. This implies that polar protic solvents (*e.g.*, water) can induce granule swelling, whereas polar aprotic solvents (*e.g.*, acetone) do not. Consequently, the type of solvent affects the effective volume of the slurry. As the solvent evaporates, the layer contracts significantly more with water than with acetone, leading to different levels of cohesive energy buildup and variations in the crack area. The cohesive energy density can be estimated from the ratio of the energy of vaporization and the molar volume of the solvent through the the Hildebrand solubility parameter, δ [54]. Since the solute (cornstarch) was the same in our experiments, we focus on the solvents to assess the influence of cohesive energy in the slurries. This parameter can be decomposed into three main contributions:

$$\delta^2 = \delta_D^2 + \delta_P^2 + \delta_H^2, \tag{2}$$

where δ_D, δ_P and δ_H are the Hansen parameters (HSP) associated with (atomic) dispersion, (molecular) polar and (molecular) hydrogen bonding interactions, respectively [54]. The Kamlet-Taft parameters (KTP) also provide additional insight into swelling by describing the hydrogen-bond donor (α), hydrogen-bond acceptor (β), and dipolarity/polarizability (π^*) of solvents [55]. These parameters are shown in Table II for the different pure liquids and binary mixtures analyzed in our experiments.

A higher Hildebrand solubility parameter leads to greater cohesive energy buildup by intensifying the constrained shrinkage of the slurry during the drying process, suggesting that higher values of δ can lead to a higher fracture density (*i.e.*, smaller cells) and more prominent crack openings, which release accumulated cohesive energy. Indeed, Fig. 9a) shows that the crack area increases nearly lineraly with δ, and, due to the presence of hydroxyl (OH) groups in starch, the δ_H value of the solvents is clearly the parameter that exerts the greatest contribution [Fig. 9b)]. Additionally, Fig. 9c) shows that A_{cr} also increases with the solvent ability to donate hydrogen bonds, given by α. The fact that acetone is not properly described by the same trend is because this solvent leaks of hydroxil groups and cannot donate a proton in a solvent-to-solute hydrogen bond [55]. The marked dependence of A_{cr} on the atomic/molecular interactions helps to understand why this geometric parameter is so relevant for solvent classification.

7. Estimating physicochemical properties from fracture patterns

The connection between geometric pattern features and microscopic-level interactions discussed in the previous sec-

TABLE III. Classification of physicochemical properties using the four-feature set $(\lambda, A_N, P_N, A_{\mathrm{cr}N})$ and $N = 60$ neurons. Eight hidden layers are used to estimate the six-property set $(\sigma, \rho, \eta, \delta_D, \delta_P, \delta_H)$, while five hidden layers are used to estimate the three-property set (α, β, π^*). (0.00 denotes an error < 0.005.)

Property / Liquid	Water	$80/20\%$	$20/80\%$	Ethanol	Acetone
σ (mN/m)	68.16 ± 11.06	41.15 ± 9.96	24.26 ± 1.99	21.85 ± 0.17	22.99 ± 0.21
ρ (g/cm^3)	0.9938 ± 0.0113	0.9680 ± 0.0126	0.8410 ± 0.0202	0.7858 ± 0.0014	0.7843 ± 0.0006
η (mPa·s)	0.9970 ± 0.2890	1.6913 ± 0.2675	1.7008 ± 0.2119	1.0897 ± 0.0254	0.3087 ± 0.0155
δ_D (MPa$^{1/2}$)	15.52 ± 0.10	15.56 ± 0.06	15.71 ± 0.16	15.79 ± 0.06	12.51 ± 0.05
δ_P (MPa$^{1/2}$)	15.77 ± 0.56	14.40 ± 0.62	10.03 ± 0.45	8.81 ± 0.04	10.40 ± 0.04
δ_H (MPa$^{1/2}$)	41.72 ± 1.85	37.14 ± 2.01	23.20 ± 1.63	19.39 ± 0.26	7.04 ± 0.16
α	1.17 ± 0.02	1.14 ± 0.02	0.95 ± 0.07	0.83 ± 0.01	0.08 ± 0.01
β	0.19 ± 0.03	0.23 ± 0.03	0.54 ± 0.07	0.77 ± 0.00	0.48 ± 0.00
π^*	1.08 ± 0.02	1.04 ± 0.03	0.75 ± 0.07	0.54 ± 0.00	0.71 ± 0.00

tion suggests that the proposed Deep learning protocol not only classifies patterns, but is also indirectly detecting the mechanical consequences of solute-solvent chemical affinity. Let us now describe a possible application of our study, specifically, an estimation of the physicochemical properties of solvents based on the morphological features of the final fracture patterns.

To reach this goal, the physicochemical properties are defined as output variables $(P_1, \ldots, P_9)$, while a linear transfer function $y_i = x_i$ is used as the activation function in the output layer to obtain free parameter values. Subsequently, the neural network is trained applying the Levenberg-Marquardt (LM) backpropagation algorithm using the data of Tables I and II, to iteratively adjusts weights and biases to minimize errors. Data adquisition and network architecture remain unchanged. First, we trained the neural network using all the data set. After an implicit classification using a 5-fold cross-validation (80% training, 20% test), we obtained the data shown in Table III. In line with the traditional classification (described in Secs. 5 and 6), the largest deviations are observed for water and the 80/20% water/ethanol. Nevertheless, most estimates have low error, typically below 2%. This indicates that the association of images of the fracture patterns with the physicochemical parameters is possible. After such corroboration, we estimated the physicochemical properties for binary solvents using the model trained exclusively with single solvents. The results are shown in Table IV. Although the model is not so accurate in determining some macroscopic properties, the microscopic properties of two-component solvents, as the Hansen and Kamlet-Taft parameters, can be estimated within a reasonable error ($< 15\%$).

TABLE IV. Estimation of physicochemical properties of binary solvents based on the analysis of patterns obtained with single solvents, using the four-feature set $(\lambda, A_N, P_N, A_{\mathrm{cr}N})$ and $N = 60$ neurons. Two hidden layers are used to estimate each three-property set: (σ, ρ, η), $(\delta_D, \delta_P, \delta_H)$ and (α, β, π^*), respectively.

Property / Liquid	$80/20\%$	$20/80\%$
σ (mN/m)	69.67 ± 4.23	32.90 ± 11.67
ρ (g/cm^3)	0.9822 ± 0.0161	0.8347 ± 0.0342
η (mPa·s)	0.8576 ± 0.0673	0.9482 ± 0.1648
δ_D (MPa$^{1/2}$)	15.42 ± 0.41	15.38 ± 0.60
δ_P (MPa$^{1/2}$)	15.65 ± 0.56	10.53 ± 1.19
δ_H (MPa$^{1/2}$)	40.49 ± 2.4	22.69 ± 6.51
α	1.12 ± 0.12	0.82 ± 0.22
β	0.20 ± 0.04	0.61 ± 0.10
π^*	1.05 ± 0.04	0.68 ± 0.12

8. Conclusions

We developed a protocol that integrates image analysis, statistics, and Deep learning techniques to classify fracture patterns of cornstarch with five different solvents, specifically focused on improving the accuracy in determining the solvent used in a desiccation process. First, the fracture patterns were characterized based on morphological features. Then, frequency histograms were generated from a normalized dataset and used to train a large number of MLP neural network variants. Our results show that: (1) classification accuracy improves when the number of neurons decreases progressively across hidden layers; (2) crack area is the most informative feature for solvent identification; and (3) accuracy is further enhanced when this parameter is combined with additional morphological features. To balance performance and computational efficiency, the four-feature set $(\lambda, A_N, P_N, A_{\mathrm{cr}N})$ is recommended, achieving an average accuracy of $96(\pm 1)\%$ in identifying the solvent in starch-liquid desiccation processes. These findings suggest that existing classification approaches across science, engineering, and medicine, often based on single parameters, could benefit from adopting similar protocols to determine optimal feature sets. Finally, we provide a microscopic perspective in which a linear dependence of the crack Area on the cohesive energy of hydrogen bonds of the solvent and on its ability to donate hydrogen bonds was found. Based on that, we propose that the physicochem-

ical properties of two-component solvents can be estimated indirectly using a model trained on patterns obtained from individual components.

Appendix

A. Origin of model confusion

As discussed in Sec. 6, most of individual features lead to less accurate results in the classification than a set of features, but in some cases, in particular $A_{\rm cr}$, a single parameter can perform better than most of features sets. This can be explained by analyzing the confusion matrices, which hide information about fracture pattern morphology and solute-solvent physicochemical interactions. The discriminative capacity of the model depends on morphological characteristics (see Fig. 7), but this is compromised when all solvents are included. Furthermore, the model accuracy is evaluated using confusion matrices for each feature. Figure 10 shows the histograms and confusion matrices for three features, sorted from the lowest accuracy (corresponding to ordering) to the highest accuracy (corresponding to crack area). A visual inspection of the input data suggests that the main reason for low accuracy is the overlap between frequency histograms, while well differentiated histograms lead to high accuracy. Nevertheless, the discriminative capacity of the model is compromised in the case of well-defined class pairs: (a/d, b/e, c/e). For all other class pairs, the error is less than 4%, regardless of the overlap in the input data. For instance, (c/a) has 0 % error for these three features despite the histograms overlap. This implies that the accuracy of the model depends not only on the morphology of the fracture patterns, but also on the solute-solvent physicochemical interactions. These interactions play an important role in classification, even though they are not explicitly included in the model. Since the solute (cornstarch) was the same in our experiments, it can be concluded that the model's accuracy also depends on the similarity of the physicochemical properties of the solvents. For this reason, we propose a distance metric M based on the physicochemical properties of solvent pairs to explain which pairs of classes compromise the model's overall accuracy, in order to map the physicochemical space of the solvents to the space of the confusion matrix.

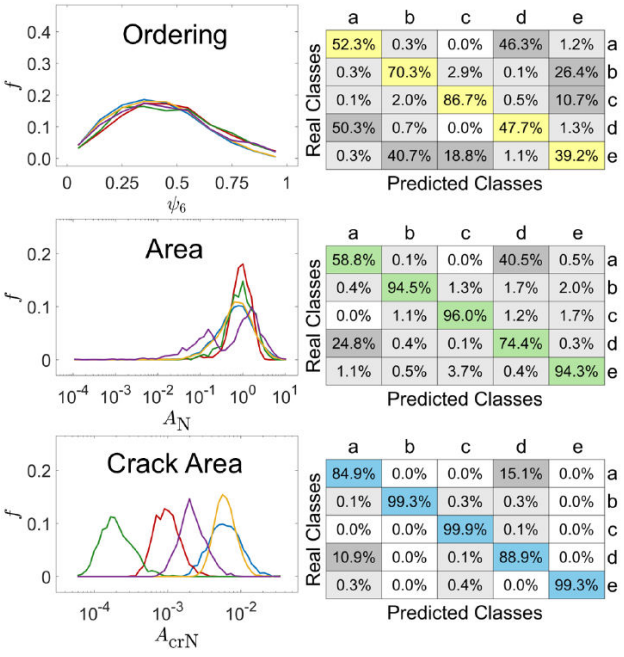


FIGURE 10. Frequency histograms and corresponding confusion Matrices for ordering (ψ_6), area (A_N) and crack area (A_{crN}). Corresponding solvents are: (a) water –, (b) ethanol –, (c) acetone –, (d) 80/20% water/ethanol – and (e) 20/80% water/ethanol –. Same labels are used in the matrices to indicate the real and predicted solvent in rows and columns, respectively. In a confusion matrix, the colored diagonal shows the correct predictions, while elements out of the diagonal indicate the percentage of error in the classification between pairs of classes.

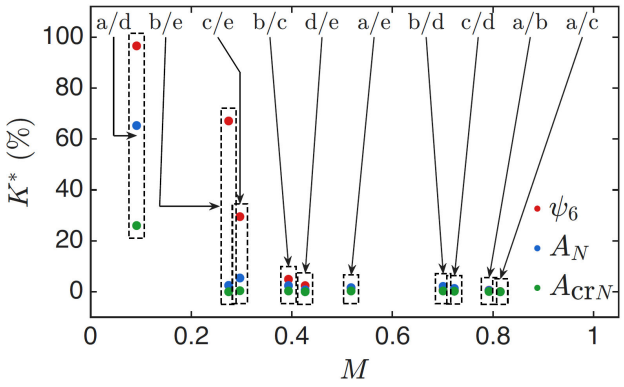


FIGURE 11. Correlation of the model confusion K^* and the metric M given by Eqs. (A.1) for ψ_6 (red), A_N (blue), and A_{crN} (green) using the values of the physicochemical properties given in Table II. Upper labels indicate the corresponding class pairs.

In this context, M was defined as:

$$M(i,j) = \sum_{k=1}^{9} \omega_k \cdot d_k(i,j), \tag{A.1a}$$

where

$$d_k(i,j) = \frac{|P_k(i) - P_k(j)|}{\max\limits_{p,q} |P_k(p) - P_k(q)|}, \tag{A.1b}$$

and

$$1 = \sum_{k=1}^{9} \omega_k. \tag{A.1c}$$

Here, P denotes the physicochemical properties of Tables I and II, i and j denote different solvents, and $\omega_k \geq 0$ are the weights for each physicochemical property $k = 1, \ldots, 9$ $(\sigma, \rho, \eta, \delta_D, \delta_P, \delta_H, \alpha, \beta, \pi^*)$.

The model confusion is defined as $K^*(i,j) = K(i,j) + K(j,i)$, where $K(i,j)$ represents the percentage error between class pairs in the confusion matrix. In this context, the aim is to establish an inverse correlation whereby, as $M \to 0$, there is a high confusion $(K^* \to 100\%)$, and as $M \to 1$, there is low confusion $(K^* \to 0\%)$. Thus,

we look for the combination of weights such that the Spearman's correlation coefficient r_s (which determines the degree to which two variables are monotonically related) tends to (-1) [57,58]. The combination that most faithfully reproduces the descending order of the model confusion is given by $(w_{\delta_H}, w_\alpha, w_{\pi^*}) = (0.20,\, 0.20,\, 0.60)$, with the remaining weights equal to zero. Using these values, we compute $M(i,j)$ using Eqs. (A.1), and $K^*(i,j)$ using the percentages indicated in the confusion matrices of Fig. 10. Figure 11 shows $K^*(i,j)$ vs $M(i,j)$. Indeed, $K^*(i,j)$ decreases as M increases, and it allows to determine the most relevant cases in which the model's discriminatory capacity is compromised (mainly for a/d, b/e and c/e), as discussed previously. Additionally, K^* and M follow strong (negative) correlation for ψ_6 and A_N (corresponding to $r_s = -0.9879$ and -0.9030, respectively), while $A_{\mathrm{cr}N}$ shows moderate correlation $(r_s = -0.4536)$. These results indicate that the neural network successfully encodes relationships between the physicochemical parameters based on the frequency histograms. Therefore, the microscopic properties play a more relevant role for a correct classification than macroscopic ones. If the microscopic properties considered in this study are very similar, the confusion will be high, independently of how close the macroscopic properties are. For instance, ethanol and acetone have very similar values of σ and ρ (see Table I) but dissimilar values of δ_H and α (see Table II) and the corresponding confusion K^* is very low (see class pair b/c in Fig. 11). Consequently, the model accuracy depends on solute-solvent molecular interactions associated to the ability of forming hydrogen bonds and effective polarity.

Acknowledgments

The authors gratefully acknowledge financial support from CONACyT Mexico (now SECIHTI) and VIEP-BUAP project 2024 and 2025. J. I. M. C. acknowledges Ph.D. scholarship 1079089 ("Becas nacionales CONAHCyT 2024").

1. F. Moreh, *et al.*, Deep neural networks for crack detection inside structures, *Sci. Rep*. **14** (2024) 4439, https://doi.org/10.1038/s41598-024-54494-y+
2. T. Mashayekhbakhsh *et al.*, SRU-Net: a novel spatiotemporal attention network for sclera segmentation and recognition, Pattern *Anal. Applic.* **27** (2024) 90, https://doi.org/10.1007/s10044-024-01301-z
3. J. Wang, M. Zhao, and C. Xia, An improved classification diagnosis approach for cervical images based on deep neural networks, *Pattern Anal. Applic.* **27** (2024) 79, https://doi.org/10.1007/s10044-024-01300-0
4. G. V. Ponomarev *et al*., ANA HEp-2 cells image classification using number, size, shape and localization of targeted cell regions, *Pattern Recognit*. **47** (2014) 2360, https://doi.org/10.1016/j.patcog.2013.09.027
5. G. V. Ponomarev and M. D. Kazanov, Classification of ANA HEp-2 slide images using morphological features of stained patterns, *Pattern Recognit. Lett*. **82** (2016) 79, https://doi.org/10.1016/j.patrec.2016.03.010
6. R. Nosaka and K. Fukui, HEp-2 cell classification using rotation invariant co-occurrence among local binary patterns, *Pattern Recognit*. **47** (2014) 2428, https://doi.org/10.1016/j.patcog.2013.09.018
7. S. Umer, B. C. Dhara, and B. Chanda, Iris recognition using multiscale morphologic features, *Pattern Recognit. Lett*. **65** (2015) 67, https://doi.org/10.1016/j.patrec.2015.07.008
8. Y. Wang *et al*., Learning the crystal structure genome for property classification, *Phys. Rev. Res*. **4** (2022) 023029, https://doi.org/10.1103/PhysRevResearch.4.023029
9. M. Fan, Q. Wang, and B. van der Waal, Wafer defect patterns recognition based on OPTICS and multi-label classification, In 2016 IEEE Advanced Information Management, Communicates, Electronic and Automation Control Conference (IMCEC) (2016) pp. 912-915, https://doi.org/10.1109/IMCEC.2016.7867343.
10. J. Choi and D. Suh, A depthwise convolutional neural network model based on active contour for multi-defect wafer map pattern classification, *Eng. Appl. Artif. Intell*. **139** (2025) 109707, https://doi.org/10.1016/j.engappai.2024.109707
11. I. U. Vakarelski *et al.*, Assembly of Gold Nanoparticles into Microwire Networks Induced by Drying Liquid Bridges, *Phys. Rev. Lett*. **102** (2009) 058303, https://doi.org/10.1103/PhysRevLett.102.058303
12. M. Ancheyta-Palacios *et al*., Dried Droplets of Diluted Blood to Detect a High Concentration of Lipids, *Processes* **11** (2023), https://doi.org/10.3390/pr11072047
13. J. Lasser *et al*., Salt Polygons and Porous Media Convection, *Phys. Rev. X* **13** (2023) 011025, https://doi.org/10.1103/PhysRevX.13.011025
14. P. Bacchin *et al.*, Drying colloidal systems: Laboratory models for a wide range of applications, *Eur. Phys. J. E* **41** (2018) 1, https://doi.org/10.1140/epje/i2018-11712-x
15. N. Mangold, High latitude patterned grounds on Mars: Classification, distribution and climatic control, *Icarus* **174** (2005) 336, https://doi.org/10.1016/j.icarus.2004.07.030
16. X. Ma, J. Lowensohn, and J. C. Burton, Universal scaling of polygonal desiccation crack patterns, *Phys. Rev. E* **99** (2019) 012802, https://doi.org/10.1103/PhysRevE.99.012802
17. A. Montigny, D. Walwer, and C. Michaut, The origin of hierarchical cracks in floor-fractured craters on Mars and the

Moon, *Earth Planet. Sci. Lett*. **600** (2022) 117887, https://doi.org/10.1016/j.epsl.2022.117887

18. W. Rapin *et al*., Sustained wet-dry cycling on early Mars, *Nature* **620** (2023) 299, https://doi.org/10.1038/s41586-023-06220-3

19. P. Pina *et al*., Polygonal terrains on Mars: A contribution to their geometric and topological characterization, *Planet. Space Sci.* **56** (2008) 1919, https://doi.org/10.1016/j.pss.2008.09.020

20. T. Choudhury and S. Costa, Prediction of Parallel Clay Cracks Using Neural Networks - A Feasibility Study, In S. Hemeda and M. Bouassida, eds., Contemporary Issues in Soil Mechanics (Springer International Publishing, Cham, 2019) pp. 214-224, https://doi.org/10.1007/978-3-030-01941-9_19.

21. L. Goehring, Evolving fracture patterns: columnar joints, mud cracks and polygonal terrain, *Phil. Trans. R. Soc. A* **371** (2013) 20120353, https://doi.org/10.1098/rsta.2012.0353

22. T. S. K. Sasa, Pattern Selection of Cracks in Directionally Drying Fracture, *Jpn. J. Appl. Phys*. **36** (1997) 391, https://doi.org/10.1143/JJAP.36.391

23. C. Allain and L. Limat, Regular Patterns of Cracks Formed by Directional Drying of a Collodial Suspension, *Phys. Rev. Lett*. **74** (1995) 2981, https://doi.org/10.1103/PhysRevLett.74.2981

24. W. P. Lee and A. F. Routh, Why Do Drying Films Crack?, *Langmuir* **20** (2004) 9885, https://doi.org/10.1021/la049020v

25. M. D. Choudhury *et al*., Effect of chloride salts on desiccation cracks in bentonite, *Colloid Polym. Sci.* **304** (2026) 823-836, https://doi.org/10.1007/s00396-026-05570-4

26. L. Pauchard, B. Abou, and K. Sekimoto, Influence of Mechanical Properties of Nanoparticles on Macrocrack Formation, *Langmuir* **25** (2009) 6672, https://doi.org/10.1021/la9001384

27. C.-S. Tang *et al*., Desiccation and cracking behaviour of clay layer from slurry state under wetting-drying cycles, *Geoderma* **166** (2011) 111, https://doi.org/10.1016/j.geoderma.2011.07.018

28. Y. Akiba *et al*., Morphometric analysis of polygonal cracking patterns in desiccated starch slurries, *Phys. Rev. E* **96** (2017) 023003, https://doi.org/10.1103/PhysRevE.96.023003

29. A. Roy *et al*., Combinatorial topology and geometry of fracture networks, *Phys. Rev. E* **105** (2022) 034801, https://doi.org/10.1103/PhysRevE.105.034801

30. S. Bohn *et al*., Hierarchical crack pattern as formed by successive domain divisions. II. From disordered to deterministic behavior, *Phys. Rev. E* **71** (2005) 046215, https://doi.org/10.1103/PhysRevE.71.046215

31. S. Bohn, L. Pauchard, and Y. Couder, Hierarchical crack pattern as formed by successive domain divisions., *Phys. Rev. E* **71** (2005) 046214, https://doi.org/10.1103/PhysRevE.71.046214

32. K. F. DeCarlo and N. Shokri, Effects of substrate on cracking patterns and dynamics in desiccating clay layers, *Water Resour. Res.* **50** (2014) 3039, https://doi.org/10.1002/2013WR014466

33. J. Baer, T. Kent, and S. Anderson, Image analysis and fractal geometry to characterize soil desiccation cracks, *Geoderma* **154** (2009) 153, https://doi.org/10.1016/j.geoderma.2009.10.008

34. H.-A. Crostack *et al*., Analysis of crack patterns in drying corn starch by in-situ radiography and X-ray computer tomography, *Exp. Mech.* **52** (2012) 917, https://doi.org/10.1007/s11340-011-9581-1

35. L. Goehring, S.W. Morris, and Z. Lin, Experimental investigation of the scaling of columnar joints, *Phys. Rev. E* **74** (2006) 036115, https://doi.org/10.1103/PhysRevE.74.036115

36. L. Goehring, Drying and cracking mechanisms in a starch slurry, *Phys. Rev. E* **80** (2009) 036116, https://doi.org/10.1103/PhysRevE.80.036116

37. J. Liaudat and S. Muraro, Drying of silty soil treated with superabsorbent hydrogels: Retention behaviour and cracking, *Eng. Geol.* **331** (2024) 107433, https://doi.org/10.1016/j.enggeo.2024.107433

38. F. Bu *et al*., Enhancement of water-retaining property and cracking resistance of soil under wetting-drying cycles: Synergistic effect of sisal fiber and polyacrylamide, *Constr. Build. Mater*. **435** (2024) 136841, https://doi.org/10.1016/j.conbuildmat.2024.136841

39. G. Vazquez, E. Alvarez, and J. M. Navaza, Surface Tension of Alcohol + Water from **20 to 50** C, *J. Chem. Eng. Data* **40** (1995) 611, https://doi.org/10.1021/je00019a016

40. A. Cervantes-Álvarez *et al*., Air entrainment and granular bubbles generated by a jet of grains entering water, *J. Colloid Interface Sci.* **574** (2020) 285, https://doi.org/10.1016/j.jcis.2020.04.009

41. S. Enders, H. Kahl, and J. Winkelmann, Surface Tension of the Ternary System Water + Acetone + Toluene, *J. Chem. Eng. Data* **52** (2007) 1072, https://doi.org/10.1021/je7000182

42. B. González *et al*., Density, dynamic viscosity, and derived properties of binary mixtures of methanol or ethanol with water, ethyl acetate, and methyl acetate at T=(293.15, 298.15, and 303.15)K, *J. Chem. Thermodyn.* **39** (2007) 1578, https://doi.org/10.1016/j.jct.2007.05.004

43. R. M. Pires *et al*., Viscosity and Density of Water + Ethyl Acetate + Ethanol Mixtures at 298.15 and 318.15 K and Atmospheric Pressure, *J. Chem. Eng. Data* **52** (2007) 1240, https://doi.org/10.1021/je600565m

44. F. López-González, F. Pacheco-Vázquez, and F. Donado, Ordering of a granular layer of cubes under strain-induced shear and vibration, *Phys. A* **620** (2023) 128768, https://doi.org/10.1016/j.physa.2023.128768

45. J.-Y. Kim, *et al*., Classification and concentration estimation of CO and NO2 mixtures under humidity using neural network-assisted pattern recognition analysis, *J. Hazard. Mater*. **459** (2023) 132153, https://doi.org/10.1016/j.jhazmat.2023.132153

46. L. Goehring, *et al*., Desiccation Cracks and their Patterns: Formation and Modelling in Science and Nature (Wiley-VCH, Weinheim, Germany, 2015), pp. 69-144, https://doi.org/10.1002/9783527671922

47. A. A. Griffith, VI. The phenomena of rupture and flow in solids, *Phil. Trans. R. Soc. A* **221** (1921) 163, https://doi.org/10.1098/rsta.1921.0006

48. J. Beuth, Cracking of thin bonded films in residual tension, *Int. J. Solids Struct.* **29** (1992) 1657, https://doi.org/10.1016/0020-7683(92)90015-L

49. T. L. Anderson, Fracture Mechanics: Fundamentals and Applications, 4th. edition. (CRC Press, Boca Raton, FL, 2017), pp. 25-39, https://doi.org/10.1201/9781315370293.

50. L. Oyarte Gálvez, *et al*., Dramatic effect of fluid chemistry on cornstarch suspensions: Linking particle interactions to macroscopic rheology, *Phys. Rev. E* **95** (2017) 030602, https://doi.org/10.1103/PhysRevE.95.030602

51. E. Bertoft, Understanding Starch Structure: Recent Progress, *Agronomy* **7** (2017) 56, https://doi.org/10.3390/agronomy7030056

52. M. Dogenski, *et al*., Starch-Based Aerogels Obtained via Solvent-Induced Gelation, *Gels* **6** (2020) 32, https://doi.org/10.3390/gels6030032

53. J. Clayden, N. Greeves, and S. Warren, Organic Chemistry, 2nd. edition. (Oxford University Press, Oxford, UK, 2012), pp. 29-67.

54. C. M. Hansen, Hansen Solubility Parameters: A User's Handbook, 2nd. edition. (CRC Press, Boca Raton, FL, 2007), pp. 1-38.

55. M. J. Kamlet, *et al*., Linear solvation energy relationships. 23. A comprehensive collection of the solvatochromic parameters, .alpha., and .beta., and some methods for simplifying the generalized solvatochromic equation, *J. Org. Chem.* **48** (1983) 2877, https://doi.org/10.1021/jo00165a018

56. K. A. Fletcher and S. Pandey, Solvatochromic Probe Behavior within Ternary Room-Temperature Ionic Liquid 1-Butyl-3-methylimidazolium Hexafluorophosphate + Ethanol + Water Solutions, *J. Phys. Chem. B* **107** (2003) 13532, https://doi.org/10.1021/jp0276754

57. C. Spearman, The Proof and Measurement of Association between Two Things, *Am. J. Psychol*. **15** (1904) 72, https://doi.org/10.2307/1412159

58. E. G. Olds, Distributions of Sums of Squares of Rank Differences for Small Numbers of Individuals, *Ann. Math. Statist.* **9** (1938) 133, https://doi.org/10.1214/aoms/1177732332